ADVANCED MATERIALS
www.advmat.de

Templated 2D Polymer Heterojunctions for Improved Photocatalytic Hydrogen Production

Catherine M. Aitchison, Soranyel Gonzalez-Carrero, Shilin Yao, Max Benkert, Zhiyuan Ding, Neil P. Young, Benjamin Willner, Floriana Moruzzi, Yuanbao Lin, Junfu Tian, Peter D. Nellist, James R. Durrant, and Iain McCulloch**

2D polymers have emerged as one of the most promising classes of organic photocatalysts for solar fuel production due to their tunability, charge-transport properties, and robustness. They are however difficult to process and so there are limited studies into the formation of heterojunction materials incorporating these components. In this work, a novel templating approach is used to combine an imine-based donor polymer and an acceptor polymer formed through Knoevenagel condensation. Heterojunction formation is shown to be highly dependent on the topological match of the donor and acceptor polymers with the most active templated material found to be between three and nine times more active for photocatalysis than its constituent components. Transient absorption spectroscopy reveals that this improvement is due to faster charge separation and more efficient charge extraction in the templated heterojunction. The templated material shows a very high hydrogen evolution rate of >20 mmol h^{-1} m^{-2} with an ascorbic acid hole scavenger but also produces hydrogen in the presence of only water and a cobalt-based redox mediator. This suggests the improved charge-separation interface and reduced trapping accessed through this approach could be suitable for Z-scheme formation.

1. Introduction

The cost of low-carbon electricity has fallen dramatically over the past two decades from rapid advances in photovoltaics and wind power and it is now cheaper to generate renewable electricity than it is to build new fossil fuel-based power stations.[1] However, 60% of global energy demands are fuel-based rather than electrical[2] and low-emission replacements to fossil fuel-derived chemical fuels for transport, residential heating, and industrial applications lag significantly behind their electrical counterparts. Hydrogen is a highly suitable energy vector for many of these applications and the interest in "green" methods of production is substantial.

Since the discovery that carbon nitride can drive photocatalytic hydrogen production from water,[3] organic semiconductors have gained increasing interest in the field of solar fuel production.[4,5] This field has been traditionally dominated by inorganic semiconductors, particularly wide-bandgap metal oxides,[6–8] but the chemical tunability of organic conjugated polymers and the ability to easily form materials with a range of different bandgaps allows for photocatalysts that can absorb a wider proportion of solar irradiation. Carbon nitrides are the most widely studied organic polymers for this application with strategies such as doping, microstructural processing and dye loading commonly employed to improve photocatalytic activity.[9] However, these materials are formed via irreversible high-temperature condensation reactions and the greatest step changes in activity have been found by switching to urea precursors[10–12] and by fabricating using ionothermal molten salt procedures.[11,13,14] More recently, conjugated cross-linked polymers,[15–18] linear polymers[19,20] and covalent organic frameworks (COFs)[21–24] have also been shown to be promising material classes for proton reduction. Hydrogen evolution rates have increased by several orders of magnitude in the last 10 years due to a growing understanding of how to optimize properties such as morphology[25,26] and wettability[27,28] as well as the importance of balancing sometimes competing factors such as light absorption and driving force.[29] Sheet-like 2D polymers are particularly promising hydrogen evolution photocatalysts with some of the highest efficiencies in the field; carbon nitride nanosheets

C. M. Aitchison, M. Benkert, B. Willner, F. Moruzzi, Y. Lin, J. Tian, I. McCulloch
Department of Chemistry
University of Oxford
12 Mansfield Road, Oxford OX1 3TA, UK
E-mail: catherine.aitchison@chem.ox.ac.uk; iain.mcculloch@chem.ox.ac.uk
S. Gonzalez-Carrero, S. Yao, J. R. Durrant
Department of Chemistry and Centre for Processable Electronics
Imperial College London
Exhibition Road, London SW7 2AZ, UK
Z. Ding, N. P. Young, P. D. Nellist
Department of Materials
University of Oxford
16 Parks Road, Oxford OX1 3PH, UK

The ORCID identification number(s) for the author(s) of this article can be found under https://doi.org/10.1002/adma.202300037

DOI: 10.1002/adma.202300037

can now reach external quantum efficiencies (EQEs) of 60%[11] whilst a highly exfoliated and crystalline imine-based COF was recently found to show EQEs of over 80%.[30] 2D materials have also been shown to be robust photocatalysts with sustained activity over a month.[31]

Whilst such 2D organic materials have very high efficiency for proton reduction, these tend to be single-component materials incapable of efficient charge separation and typically only display significant hydrogen evolution rates when employed with fast-acting hole scavengers such as TeOA.[32] Other materials have been shown to be capable of generating long-lived charge-separated species but these are frequently stabilized trap states that are catalytically inactive.[33] A significant barrier to overall water splitting is that the oxidation of water or indeed other sustainable electron donors is generally slow/kinetically challenging[34,35] and so catalytically active charge-separated species cannot be generated by quenching. Instead, charge separation must be achieved on the photocatalyst itself. There are many studies that aim to achieve this by incorporating "donor–acceptor" or "push–pull" motives into the chemical structures of organic semiconductors.[36–42] Whilst this has been shown to lower exciton binding energy, the lack of special separation between the electron donating and electron accepting sections of such structures means that geminate recombination is still a significant loss pathway.

An alternative route to improve charge separation is to use two different semiconductors to form a heterojunction. The field of organic photovoltaics (OPV) contains myriad examples of such systems which use pristine, or more commonly, blended films of donor and acceptor organic semiconductors to efficiently generate charge-separated species upon photoexcitation.[43] Recently there has been a move to translate this into photocatalysis by forming water-dispersible blended heterojunction nanoparticles via nanoprecipitation[44,45] or nanoemulsion[46] techniques. Aside from increasing sacrificial hydrogen production rates, we have recently demonstrated that blended nanoparticles of such materials are also capable of producing long-lived polarons without adding any kind of sacrificial agents or cocatalysts (which can act as electron sinks) a key step toward non-sacrificial hydrogen production.[47]

Unlike the flexible semiconductors used in nanoemulsion blends, 2D polymers have rigid sheet-like structures which are essentially fixed during synthesis. They are also insoluble in organic solvents and thus cannot be processed post-synthesis using the same techniques as typical OPV semiconductors. However, 2D materials have the potential to combine long exciton diffusion lengths,[48] high conductivity,[49] porosity, and extended light absorption[50] with molecular tunability and so are also a promising class of organic semiconductors for photocatalytic proton reduction.

The sheet-like morphology of 2D polymers means that they can be polymerized or "grown" from a variety of different metal and non-metal substrates. Polymerization onto metal surfaces is typically achieved through vacuum deposition of monomers[51] and is often combined with thermal activation for non-condensation polymers.[52,53] Other surfaces, such as graphene can be templated simply by submersion into solvothermal polymerization reactions. Carbon-based substrates can rely on covalent bonds between the surface and the polymer[54] but many aromatic materials simply rely on non-covalent π-stacking interactions to direct the nucleation and growth of the polymer sheets.[55] It has been shown that COF crystals could be grown from small nanoseeds[56] in a self-templating mechanism that resulted in ordered crystalline domains up to the micrometer scale. Recently a similar technique has expanded to "heterotemplating" whereby seeds of a framework of one chemical structure can be used to template the growth of a framework with a different chemical structure, but an equivalent secondary pore structure.[57] This templating mechanism relies on through-layer π-stacking interactions that are similar to the inter-sheet interactions between the layers of "monophase" 2D polymers and provides an ideal interface for a heterojunction. In this work, we employ a templating route to generate organic donor–acceptor heterojunctions of otherwise unprocessable 2D polymers.

To avoid cross-contamination of donor and acceptor monomers, the original polymer template must be inert to the synthesis conditions of the second. It has been shown that COFs with imine linkages can be used to template analogs COFs with Knoevenagel linkages and therefore our investigations focus on these two motives. **Figure 1**. shows the structures of COF monomers M1, M2, M3, and M4. M1 and M3 are isostructural with the same node size and bond angles for the C═N or C═C bonds formed during condensation, respectively. M3 is however significantly more electron-withdrawing with three cyano groups and none of the electron-donating phenol substituents present on M1. Similarly, M2 and M4 are both linear linkers with equal lengths and condensation bond angles, but M4 has an electron-poor pyridyl unit instead of M2's phenyl and no electron-donating amine group. As such, the imine-based polymer formed from the condensation of M1 and M2, namely D1, would be expected to have considerable donor character and shallow energy levels. In comparison, the electron-deficient Knoevenagel polymer formed by condensation of M3 and M4, A1, is expected to be an acceptor with deep-lying frontier molecular orbitals (FMOs). However, the backbone conformation and packing of the two polymers should be highly similar. The matching linker and node groups mean that these materials will form 2D sheets with isostructural frameworks and are thus promising candidates for heterotemplating.

2. Results and Discussion

2.1. Development of Single Component Donor and Acceptor 2D Polymers

Polymerisation of D1 was achieved via acetic acid catalyzed imine condensation of 1,3,5-triformylphloroglucinol, M1, and 4,4″-(thieno[3,2-b]thiophene-2,5-diyl)dianiline, M2, whilst A1 was formed via base catalyzed Knoevenagel condensation of 2,4,6-trimethylbenzene-1,3,5-tricarbonitrile, M3, and 6,6″-(thieno[3,2-b]thiophene-2,5-diyl)dinicotinaldehyde, M4. Both polymers formed red powders that were insoluble in all common solvents tested including water, methanol, acetone, tetrahydrofuran, chloroform, and *N*,*N*-dimethylformamide (DMF).

Condensation of the monomers was confirmed by FT-IR (Figures S7 and S8, Supporting Information.) The D1 spectra showed the disappearance of the 1,3,5-triformylphloroglucinol

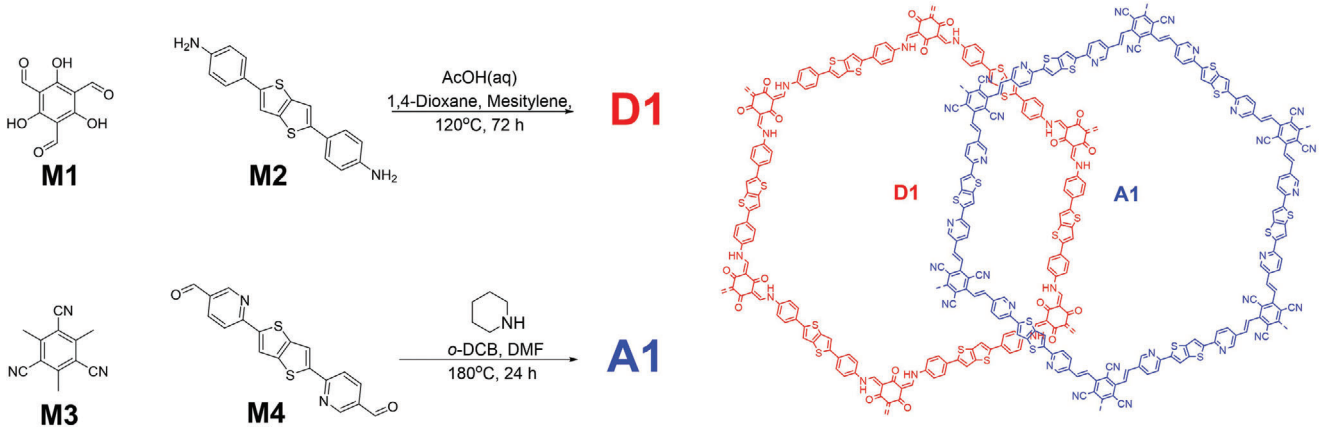

Figure 1. Synthesis and chemical structures of monomers and polymers.

C=O stretch at 1642 cm^{-1} and the growth of a new peak at 1619 cm^{-1}. This is assigned to a new C=O stretch and indicates that the β-enol imine bonds in D1 undergo enol-keto tautomerization (Figure S10, Supporting Information).[58] A1 showed the disappearance of the 6,6′-(thieno[3,2-b]thiophene-2,5-diyl)dinicotinaldehyde C=O stretch at 1682 cm^{-1} and retained a C≡N stretch peak at 2368 cm^{1} indicating the nitrile groups are stable to the polymer synthesis conditions. The thermal stability of the polymers was tested by thermogravimetric analysis in nitrogen (Figure S19, Supporting Information) and showed high decomposition onsets of 458 and 467 °C for D1 and A1 respectively.

The partially reversible condensation bonds in these polymers can lead to highly ordered crystalline structures, however, analysis of D1 and A1 by PXRD showed only low-intensity peaks (Figure S11, Supporting Information) suggesting the materials are not crystalline over large lengths scales. TEM did reveal that D1 and A1 formed thin sheet-like particles (Figure S12, Supporting Information) of between 100 and 1000 nm.

The absorption spectra of the polymers were recorded in DMF suspension (Figure S20, Supporting Information) The imine polymer D1 was found to have an onset at 648 nm whilst A1 was blue-shifted in comparison with an onset of 607 nm. Photoelectron emission spectra in air (PESA) were conducted on the single component materials (Figures S23 and S24, Supporting Information.) to determine their ionization potentials (IPs). The IP of D1 was determined as −5.36 eV, whilst the electron-poor A1 has an IP of −5.88 eV. Electron affinities (EAs) were calculated by the addition of the optical bandgap to the IP, giving −3.45 and 3.84 eV for D1 and A1, respectively. The frontier molecular orbital (FMO) energies are summarized in **Table 1**. The 0.39 eV and 0.52 eV offset between the materials LUMOs and HOMOs respectively suggest they are suitable candidates to form a type II heterojunction. In addition to PESA the redox potentials of the materials were investigated by cyclic voltammetry. In general, low film quality and conductivity of the sample lead to low signals. However, an oxidation potential for D1 could be determined, giving an IP of −5.11 eV. This 0.25 eV variation between electrochemical and photoexcitation methods of characterization is highly typical of organic conjugated polymers.[59]

Table 1. Optoelectronic properties of polymers.

Polymer [units]	λ_{onset} [nm][a)]	Optical gap [eV]	IP [eV][b)]	EA [eV][c)]
A1	648	1.91	−5.36	−3.45
D1	607	2.04	−5.88	−3.84
D2	631	1.96	−5.5	−3.54
D3	594	2.09	−5.65	−3.56

[a)] Absorption onset from UV–vis spectra of polymer in DMF suspension [b)] Calculated from PESA [c)] Calculated from the addition of IP and optical gap.

Crucially the FMO energies of both materials straddle the proton reduction potential and the ascorbic acid oxidation potential at pH 3 and pH 7 (**Figure 2.**), indicating they should be able to facilitate hydrogen production in both cases. To confirm this, photocatalysis was first conducted on single-component materials. The polymers were suspended in ascorbic acid 0.1 M with a DMF cosolvent and 3 wt% Pt cocatalyst before illumination with visible light (390–740 nm, see Supporting Information for full details). Both materials were found to evolve hydrogen linearly over the 15 h testing period (Figure 2.). D1 had a hydrogen evolution rate (HER) of 3.3 μmol h^{-1} whilst A1 had a higher HER of 9.4 μmol h^{-1} with reasonable reproducibility between polymer batches (Figure S32, Supporting Information). When the acidic scavenger solution was buffered to pH 7 with NaOH, the HER of D1 increased to 6.5 μmol h^{1}, most likely due to the increased driving force for ascorbic acid oxidation under these conditions. On the other hand, the HER of A1 decreased to 1.2 μmol $h^{1,}$ which we ascribe to the material's very small (<0.2 eV) overpotential for proton reduction at this pH. These tests supported the experimentally derived band positions and so D1 and A1 were deemed suitable candidates for templated heterojunction formation.

2.2. Development of Templated Donor–Acceptor Heterojunctions

Heterojunction template formation was first conducted in a 1:1 donor: acceptor ratio. D1 seed particles were sonicated with a mixture of M3 and M4 in DMF:*o*-DCB (1:1) and Knoevenagel condensation was then achieved via the same piperidine-catalyzed procedure as used for the formation of A1 (see Experimental Section

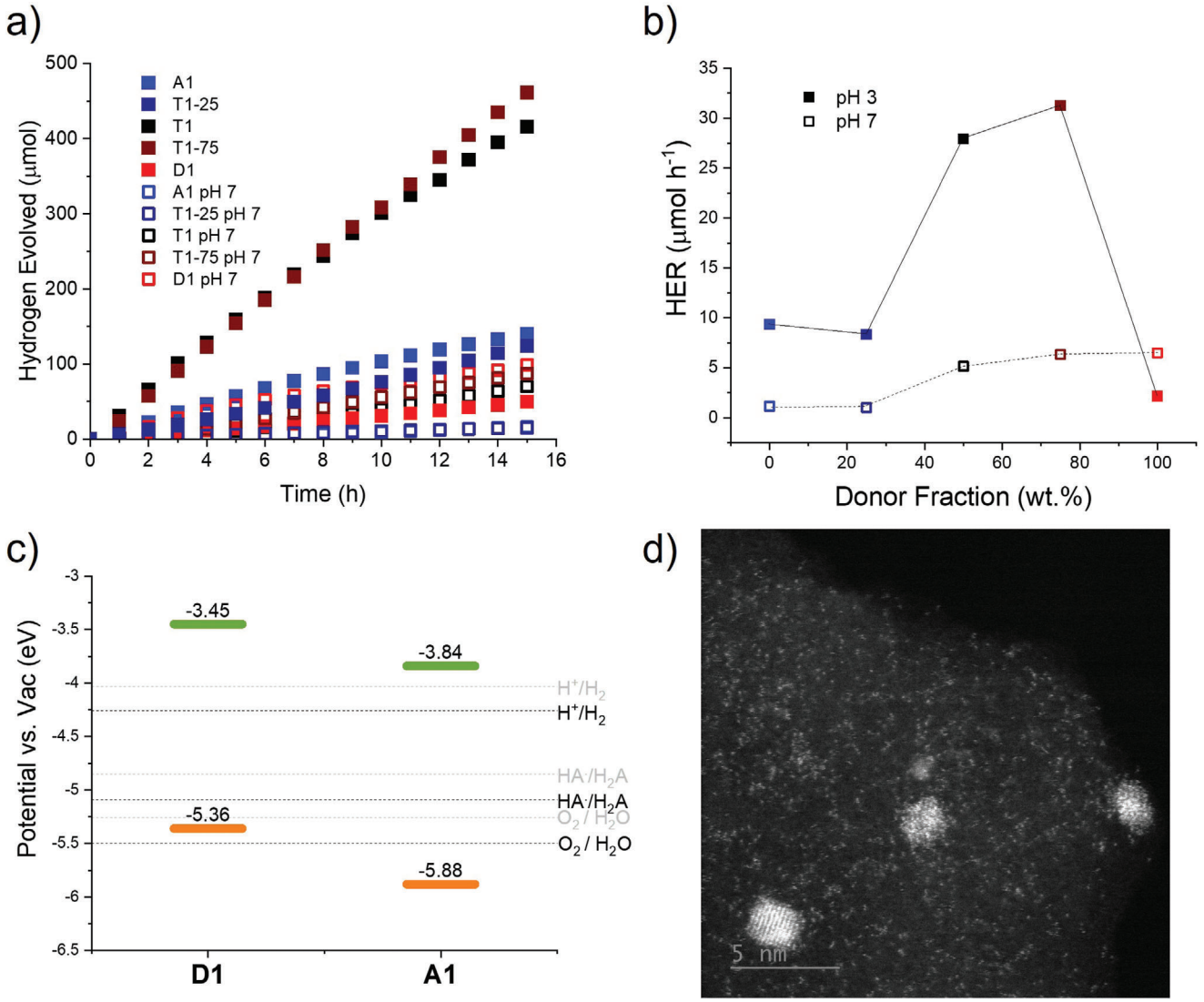

Figure 2. a) Photocatalytic hydrogen production of the polymers (5 mg) with 3 wt% Pt dispersed in DMF:water (2:5, 35 mL) with ascorbic acid (440 mg) under visible-light illumination. b) HERs of the polymers at different blend ratios at different pH, $NaOH_{(aq)}$ was used to adjust to pH 7. c) IP and EA of the polymer components compared to the proton reduction potential (H^+/H_2), water oxidation potential (O_2/H_2O) and the calculated potential of the two-hole oxidation of ascorbic acid to dehydroascorbic acid in solution (DHA/AA), at pH 3 (black lines) and at pH 7 (gray lines). All energy levels and electrochemical potentials are expressed on the absolute electrochemical scale (0 V vs standard hydrogen electrode (SHE) = −4.44 V vs vacuum). d) STEM image of T1 post photocatalysis showing deposition of Pt nanoparticles.

for full details). The resultant dark red powder, T1, (made up of 50:50 wt% D1:A1) was collected and analyzed by TGA (Figure S19, Supporting Information), and FT-IR (Figure S9, Supporting Information). T1 showed a slightly higher decomposition temperature than either component polymer of 477 °C and showed both the 1619 cm^{-1} C═O stretch associated with D1 and the C≡N stretch peak at 2368 cm^{-1} of A1. T1-25 and T1-75 were formed via the same procedure but with a 25:75 and 75:25 D1:A1 weight ratio, respectively, and showed similar IR spectra, with increases in the relative intensity of the A1 signals in T1-25 and those of D1 in T1-75. The stability of D1 to the higher temperature and basic Knoevenagel reaction conditions was checked by subjecting D1 to the templating procedure without the M3 and M4 monomers. The resulting material D1-Knov was found to retain >90% of its mass and had an almost identical UV–vis absorption profile and IR spectra to D1 (Figures S21 and S7, Supporting Information), suggesting D1 does not chemically degrade during the templation process.

UV–vis of T1, T1-25, and T1-75 (Figure S20, Supporting Information) showed absorption profiles with similar onsets to D1 but with higher absorption intensity from 400–500 nm, where the absorption maxima of A1 lies.

Similarly to A1 and D1, T1 appeared to be semicrystalline with only broad, low-intensity peaks in the PXRD spectrum (Figure. S11). Nitrogen sorption isotherms (Figure S18, Supporting Information) did show that the materials were moderately porous with BET surface areas of 244 cm^{-2} g^{-1}, 100 cm^{-2} g^{-1} and 221 cm^{-2} g^{-1} calculated for A1, D1, and T1, respectively.

A1 and T1 in particular showed a sharp adsorption increase at low pressures indicative of micropores and consistent with a proportion of the material forming the hexagonal framework structures shown in Figure 1. The microstructure of the T1 particles was analyzed by TEM and showed similar sheet-y aggregates as the single component materials (Figure 2). Photocurrent measurements were attempted on A1, D1, and T1; device architecture consisting of ITO/PEDOT:PSS/active layer/PFN-Br/Ag and ITO/ZnO/active layer/MoO_3/Ag were attempted by utilizing A1, D1, and T1 as active layers (Figure S28, Supporting Information). However, no photoresponse was observed in all three devices in both standard and inverted structure, possibly due to poor coverage of COF suspension on PEDOT:PSS and ZnO layer via drop casting or the low conductivity of the materials.

2.3. Initial Testing of Templated Donor–Acceptor Heterojunctions

T1 was tested for photocatalytic proton reduction under identical conditions to D1 and A1 and was found to give a much higher HER of 28 μmol h^{-1}. This is approximately three times the rate of A1 and more than 8 times that of D1, indicating a beneficial interaction between the two components. Interestingly a physical mixture of D1 and A1, in the same 1:1 wt% ratio as in T1, did not show the same increase in activity. Despite sonication of the D1 and A1 materials together prior to photocatalytic testing, the physical mixture gave an HER of only 5.1 μmol h^{-1}, intermediate between that of the two single components (Figure S31, Supporting Information). This suggests that the templated growth procedure used for T1 is crucial in generating an efficient charge-separation interface between the donor and acceptor polymer sheets (see analysis below). The heterojunction interface was investigated next by reversing the order of templation such that D1 was polymerized onto pre-made sheets of A1 in the same 50:50 wt% ratio. The material produced by T1rev was found to show an HER of 17 μmol h^{-1} (Figure S31, Supporting Information). This is more than twice the HER of either single component suggesting again that heterojunction formation had occurred. The significantly higher activity of T1 (in the original order of templation) meant that this system was carried forward for further testing. The results for T1 were verified with new batches of each material, with the repeats showing a similar trend in activity to the first batches (Figure S32, Supporting Information); HER for the new batches was 6.5, 8.3, and 36 μmol h^{-1} for D1, A1, and T1 respectively. Increasing the concentration of the ascorbic acid hole scavenger had only a small effect on HER; with 0.2 M and 1.0 M solutions, T1 gave HERs of 33 and 30 μmol h^{-1} (Figure S33, Supporting Information) suggesting the standard 0.1 M original conditions are within the saturated regime for this component and are not rate limiting. Testing T1 with various Pt cocatalyst loadings gave a typical "volcano" plot of activity, decreasing to 1 wt% Pt gave a HER of 19 μmol h^{-1} and increasing to 5 wt% Pt gave 4.0 μmol h^{-1}, both lower than the 28 μmol h^{-1} achieved with 3 wt% (Figure S34, Supporting Information). Changing the dispersant to a fully aqueous system (as opposed to DMF:water (2:5)) also lowered the rate to 16 μmol h^{-1} as did switching to an NMP:water (2:5) which gave an HER of 18 μmol h^{-1}. (Figure S35, Supporting Information). In the former case, the T1 polymer sheets were visibly less well dispersed than in the DMF-containing system, potentially causing lower activity. There appeared to be a tipping point between dispersibility and water concentration, however, as changing the DMF:water ratio to (5:2) lead to a decreased rate of 10 μmol h^{-1} (Figure S35, Supporting Information). The T1 sheets were well dispersed in the NMP:water system, but it was noted that even after the addition of the ascorbic acid scavenger, the pH of the solution was ≈5, higher than the other dispersants which likely reduced the driving force for proton reduction (see Section 2.5). Similarly, testing of T1 with an alternative TeOA electron donor gave a low rate HER of 0.2 μmol h^{-1} after a long induction period most likely due to the high pH of the dispersant (Figure S36, Supporting Information).

TEM imaging of the polymers showed that D1 formed slightly larger, more well-defined sheets than A1 (Figure S14, Supporting Information) and regions of both components could be observed in particles of T1 (Figure S13, Supporting Information). What appeared to be layers of acceptor partially covering the sheets of donor could be observed in this sample. This was especially evident in the sample of T1 analyzed post-catalysis where the areas of acceptor sheet have significantly higher Pt loading than the exposed donor sheet areas. Aside from Pt photodeposition (discussed below), we found little change in morphology before and after photocatalysis with all polymers forming a mix of small <200 nm sheet-like particles and larger aggregates.

Further microscopy on T1 post catalysis looked at Pt photodeposition by High Angle Annular Dark Field (HAADF) STEM. This showed that Pt was distributed relatively uniformly throughout the sample (Figure S15, Supporting Information) and that there was a large range of particle sizes from aggregates >10 nm to 1–5 nm clusters down to very small regions of Pt with sizes (ca. 0.1 nm) that indicated single atom (SA) sites (Figure 2d). SA cocatalyst loading has been observed in 2D polymers before, using the same precursor.[60] In that study, it was suggested that nitrogen atoms in the polymer backbone helped to stabilize SA to aggregation. A similar effect may be occurring in T1 whose constituent components, A1 and D1 both have potential coordinating nitrogen groups present in their structures. Analysis of the single component materials post-catalysis also showed evidence of very small, probable SA Pt sites along with the same varied Pt size distribution (Figure S16, Supporting Information) indicating that although the large surface area cocatalyst distribution most likely does play a role in T1's high activity, these must be paired with efficient charge generation and extraction to give high HERs.

The yield of Pt deposition was monitored via ICP-MS and little variation was found between materials (Table S3, Supporting Information). D1 collected by filtration after 15 h of catalysis was found to contain 2.39 wt% Pt whilst A1 and T1 contained 2.43 and 2.23 wt% respectively. T1 with 1 and 5 wt% Pt added for photocatalysis showed 0.97 and 4.03 wt% Pt had photodeposited respectively. Hole scavenger concentration also showed little effect on Pt formation with the T1 sample tested in 1 M ascorbic acid showed 2.21 wt% Pt deposition almost identical to that of the 0.1 M sample (2.23 wt%). Cosolvent addition was found to have a significant effect with the fully aqueous sample showing a higher Pt photodeposition of 2.90 wt%, whilst the sample with (2:5) NMP cosolvent contained 2.28 wt%, similar to the (2:5) DMF sample and higher than the (5:2) DMF sample of 1.62 wt% and

a fully DMF sample of 0.31 wt%. The alternative TeOA sacrificial donor was found to give the largest change in photodeposition yield with only 0.11 wt% Pt deposited of the 3 wt% added. The lower Pt loadings of the TeOA and higher cosolvent ratio samples also likely contributed to their lower activity. Pt photodeposition yields have been shown to be sensitive to organic cosolvent/electron donor type before[61] and this result again highlights the importance of analyzing photocatalytic activity in the context of deposited Pt yields rather than relying on the amount of precursor added. The photocatalytic longevity of T1 was tested over a 100 h experiment with periodic replacement of the ascorbic acid and electrolyte (Figure S37, Supporting Information). There was no decrease in activity over the first day with an HER of 31 μmol h^{-1} from hour 22 to 24 compared to 30 μmol h^{-1} from hour 2 to 4. From day 2 onwards a slow decrease in activity was observed with HER of 24 μmol h^{-1} from hour 46 to 48 and 12 μmol h^{-1} from hour 98 to 100. T1 produced a total of 2263 μmol of hydrogen during this experiment, more than 28 times the amount present in the polymer itself. Control reactions without ascorbic acid, without light, and without polymer all produced negligible amounts of hydrogen (Figure S36, Supporting Information). The control reaction without water showed low photocatalytic activity of 0.05 μmol h^{-1} reflecting the fact that ascorbic acid can act as a source of protons as well as an electron donor. A sample of T1 without any additional Pt cocatalyst gave a HER of 0.41 μmol h^{-1} it is possible that the polymer backbone can act as a site of proton reduction but it should also be noted that all 2D polymers samples contained 15–30 ppm residual Pd from the synthesis of the monomers; sufficient quantities to give proton reduction activity.[62]

2.4. Photophysical Characterization

We turned to investigate the photophysical properties of the templated polymer T1 and its constituent polymers A1 and D1. Steady-state and time-resolved photoluminescence (PL) was used to investigate the emissive state of the polymers. The dispersions of A1 and D1 showed low-intensity PL with broad emission, centered at 470 nm and 500 nm for A1 and D1, respectively, with tails extending up to 600 nm (Figure S42, Supporting Information). The origin of the emission bands in 2D polymers has been attributed to radiative recombination in the single units of the polymers.[63,64] Despite the low PL intensity of polymers, strong PL quenching (87%) was observed in T1 relative to its constituents A1 and D1, suggesting charge (or energy) transfer from the donor to the acceptor polymer in T1. Time-resolved PL studies of polymers on excitation at 404 nm showed multiexponential PL decay with an average lifetime of 1.2 ns and 1.4 ns for A1 and D1, and slightly faster in T1 of 1.1 ns, in qualitative agreement with PL quenching observed.

We subsequently explored the exciton and charge dynamics of polymers on the picosecond timescale by using ultrafast transient absorption spectroscopy (uf-TAS). **Figure 3**. shows the uf-TA spectra of A1, D1, and T1 dispersion in DMF-water excited at 450 nm and probed in the visible to NIR range. The polymer D1 exhibited a broad ground state bleaching (GSB) and photoinduced absorption (PIA) in the NIR, which decays over 500 ps and showed a residual long-lived (>6 ns). The uf-TA spectra of A1 and T1 showed similar absorption bands; at 1 ps both polymers exhibited a GSB at 550 nm and a broad PIA with maximum absorption at 700–900 nm. Interestingly, the visible spectra of the A1 polymer evolve into a band with a maximum at 625 nm over the first 100 ps and showed a long-lived decay (>6 ns) as shown in the TA kinetics in Figure 3d. (see also kinetics in the NIR range in Figure S43, Supporting Information). This broad vis-NIR PIA is also observed at a longer time scale (>10 μs, **Figure 4**.), suggesting the formation of long-lived charges in A1. The kinetics of photogenerated charges showed fluence-independent decay indicative of notable monomolecular (geminate) recombination of bound charges (Figure S44, Supporting Information). This behavior is similar to that seen in organic semiconductor heterojunctions particles and films with geminate recombination losses, limiting their efficiency.[47,65]

In polymer T1, the 625 nm absorption feature is more intense, even at 1 ps, suggesting faster charge separation in this polymer (Figure 3c.) attributed to donor–acceptor charge transfer. In addition, the decay kinetics were fluence-dependent, indicative of bimolecular recombination of separated charges (Figure S44, Supporting Information). These results suggest that the template approach improves charge separation and suppresses the charge transfer state geminate recombination.

We now focus on the μs–ms transient absorption studies of polymers in the absence or presence of sacrificial electron donor (ascorbic acid) and loaded Pt co-catalyst. The TA spectra of A1 and T1 polymers showed broad PIA (600–1000 nm) as observed in the uf-TA spectra described above, in agreement with photogenerated charges, Figure 4. and Figure S31 (Supporting Information). The polymers exhibited a power law decay with half-life (measured after 10 μs) of 145 μs and 32 μs for A1 and T1 respectively, probed in the NIR (950 nm) (Figure 4a). In contrast, no significant signal was observed in the polymer D1 in this timescale, even in the presence of Pt and ascorbic acid, indicative of faster recombination (in nanoseconds) of the photogenerated charges in D1 (Figure S45, Supporting Information). Interestingly, in the presence of the ascorbic acid hole scavenger, the kinetics of T1 showed an increase in the amplitude and the decay was 10 times slower than the kinetics in DMF-water. In the presence of a Pt electron scavenger, kinetics showed decreased amplitude and faster decay. A similar trend was observed in the presence of sodium persulfate as an electron scavenger (Figure S46, Supporting Information). The increase in the lifetime in the presence of ascorbic acid is consistent with reduced charge recombination due to hole scavenging, indicating that the positive PIA is primarily due to the absorption of photogenerated electrons in the templated polymer T1. In contrast, the TA kinetics of the A1 revealed less significative changes in the presence of ascorbic acid and Pt (Figure 4b), despite the slower recombination of charges, indicative of inefficient electron and hole extraction on the μs-s time scale, likely due to formation of deeply trapped charges. Complementary measurements at different excitation fluences showed that photogenerated electrons in T1 exhibited a power law behavior, with an increase in the TA amplitude and the α exponent of the power law, whose value was −0.22 at the highest intensity studied (Figure 4b). On the other hand, A1 showed an increase in the TA amplitude and fluence-independent α exponent, with a value of −0.11. These results are indicative of the formation of deeper traps and inactive charges in A1, in agreement

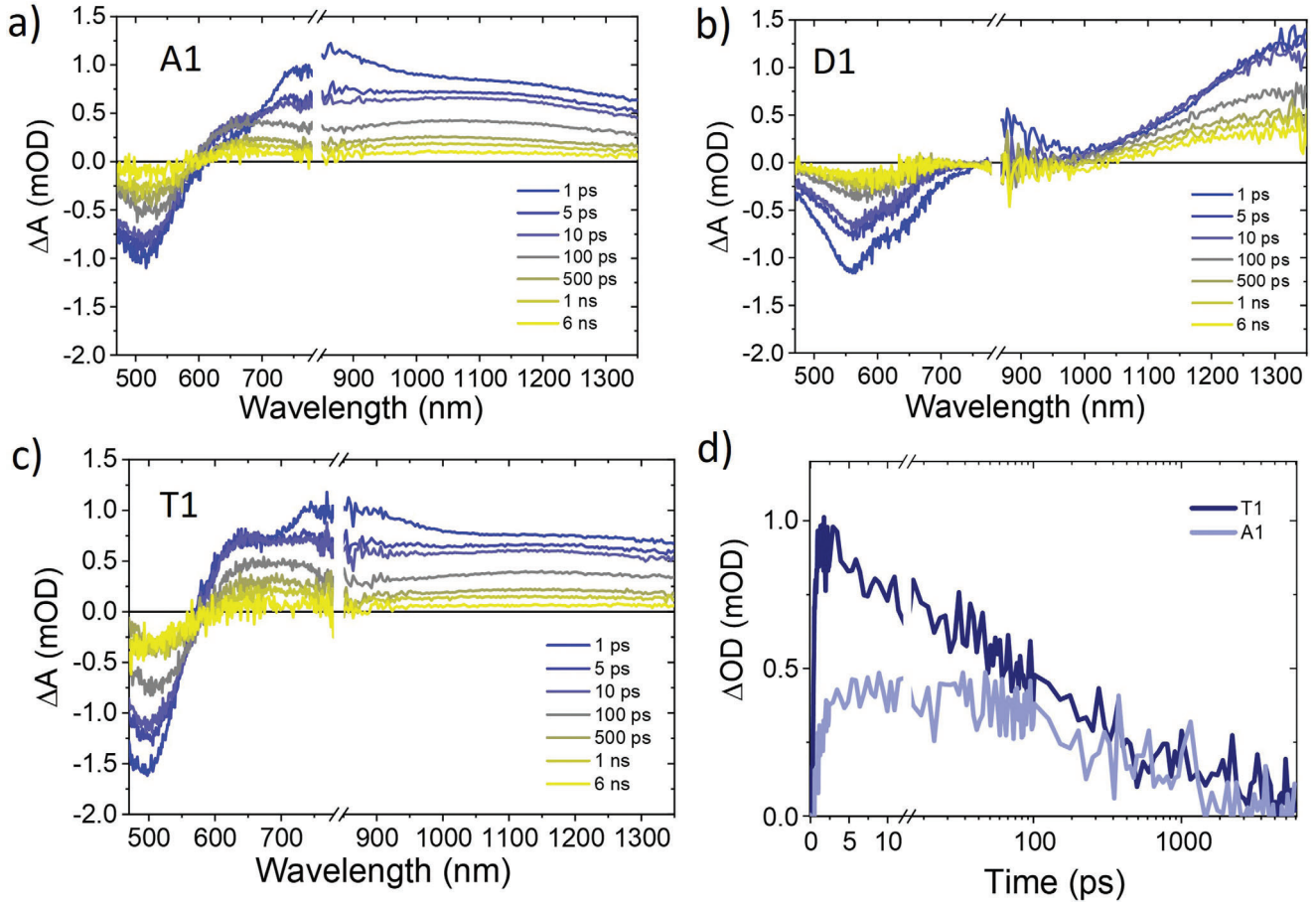

Figure 3. a–c) Ultrafast transient absorption spectra at different time delays of A1, D1, and T1 dispersions in DMF–water; excited at 450 nm and probed in the VIS and NIR (fluence: 45 μJ cm^{-2}). The samples were adjusted at the same absorbed photons. d) Comparison of transient absorption decay dynamics of A1 and T1 probed at 625 nm. The disconnect range in the transient absorption spectra axis corresponds to the switch from Vis to NIR detector (in ca. 850 nm).

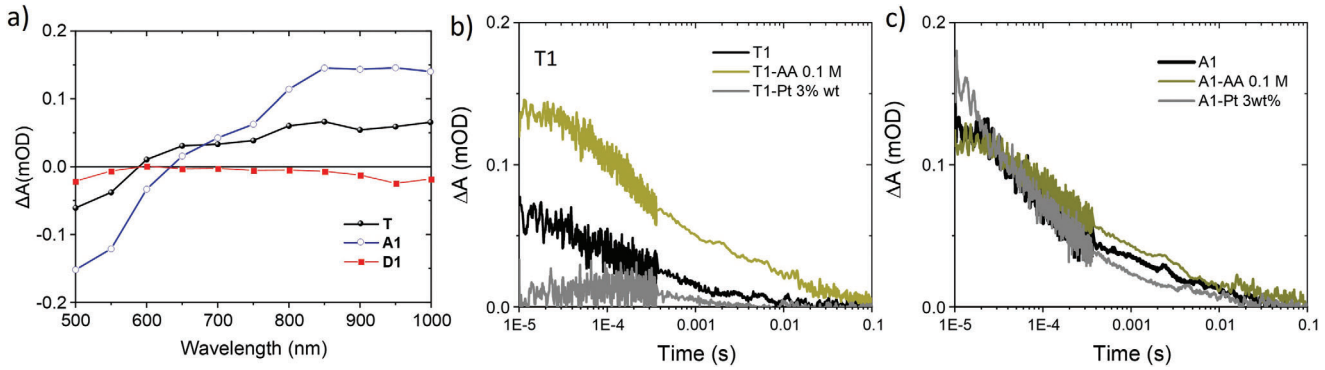

Figure 4. a) Comparison of the transient absorption spectra of T1, A1, and D1 at 10 μs delay time. b,c) Transient absorption decay dynamics of polymers T1 (b) and A1 (c) dispersions probed in the NIR (950 nm) and measured in the absence and presence of AA (0.1 M) and Pt (3 wt%). Excited at 450 nm (1 mJ cm^{-2}). Samples adjusted for the same absorbed photons.

with limited charge extraction in the presence of electron and hole scavengers.[33,66]

These μs-s TAS studies thus reveal slower charge carrier decay in polymers A1 and T1 in DMF-water compared to D1. The fast decay kinetics in polymer D1 are in agreement with the lower hydrogen evolution rate observed. In the presence of Pt and ascorbic acid, the TA kinetics revealed clearer differences in the charge carrier kinetics for polymer T1 than A1, indicating that the difference in photocatalytic activity arises from more efficient charge extraction to Pt and ascorbic acid in the templated polymer T1

compared to A1. This is consistent with the more efficient charge separation observed in the uf-TAS data for the donor–acceptor 2D polymers prepared using the template approach than in the single-component 2D polymers, facilitating efficient electron and hole extraction on slower timescales.

2.5. Further Photocatalytic Testing

To gain further insight into the interactions between the donor, the acceptor, and the redox reagents, we moved on to further photocatalytic analysis. Moderating the donor: acceptor ratio of the template gave a significant change in HER (Figure 2a). The templated material at a higher donor ratio, T1-75, showed even higher activity than T1, with a rate of 31 μmol h^{-1} which corresponds to 2.0 μmol cm^{-2} h^{-1}, higher than the highly crystalline and wettable 2D polymer FS-COF (1.6 μmol cm^{-2} h^{-1})[23] although not as high as the recently reported CYANO-CON (29 μmol cm^{-2} h^{-1}).[30]

The external quantum efficiency (EQE) of the highest-performing templated polymer was measured using a series of bandpass filters (Figure S38, Supporting Information). T1-75 showed a maximum EQE of 6.4% at 500 nm. 450 nm photons gave an EQE of 3.2% whilst lower efficiencies of, 1.8 and 1.0% were recorded for 550 and 600 nm photons, reflecting the lower absorption of the material at these wavelengths. This is amongst the highest efficiencies for 2D polymers formed via low-temperature condensation reactions; similar to the pyrene containing imine COF PY-DHBD-COF (8.4%)[67] and higher than the hydrophilic FS-COF (3.2%), the hydrazone-linked TFPT-COF (2.2%),[21] the azine based N_3-COF (0.44%)[22] and the sp^2-carbon-linked COF-JLU100 (5.13%).[68] The efficiency is however an order of magnitude lower than the 82.6% at 450 nm recently reported for the nitrile-bearing CYANO-COF.[30] In general, the efficiency of 2D polymers and COFs made up of reversible condensation linkages is slightly behind that of CMPs formed through Pd-catalyzed carbon-carbon cross-coupling and carbon nitrides which can reach EQEs of 30%[69] and >60%[11] respectively.

In contrast to T1 and T1-75, T1-25 did not show an increase in HER compared to the constituent components, with an HER of just 8.3 μmol h^{-1}. This is somewhat surprising, especially given A1's increased activity and photogenerated charge generation in comparison to D1, but can be explained by considering the microstructure of the templated material; D1 and A1 are both comprised of thin, sheet-like particles, typical of 2D polymers. The nature of the templating procedure means that layers of A1 form on both the top and the bottom of the D1 seed sheets limiting the interface of D1 and the electrolyte to the thin sheet edges or any gaps on the sheet surface not covered by A1. The more accessible hole extraction in T1 compared to A1 shown by μs TAS suggests that hole scavenging is primarily occurring on the donor sections of the material—consistent with the type II heterojunction offset shown in Figure 2c. In this case, the interface between D1 and the electrolyte is crucial for efficient photocatalytic activity. In the templated materials with high acceptor ratios, the coverage of the acceptor component on the donor sheets is more complete and thus prevents the transfer of holes to ascorbic acid. In contrast, at lower acceptor ratios, the non-coherent coverage on the donor means that holes can still be transferred efficiently to ascorbic acid. There was little difference in Pt photodeposition yields between the different ratio templates; ICP-MS showed that T1-25 and T1-75 had 2.31 and 2.42 wt% Pt respectively, similar to T1-50 (2.23 wt%).

The templated materials were also tested at pH 7. The hydrogen evolution rates for T1-25, T1, and T1-75 under these conditions were 1.0, 5.2, and 6.3 μmol $h^{-1,}$ respectively. Figure 2 shows the clear decrease in rate with acceptor ratio. These results indicate the less negative proton reduction potential at higher pH and the subsequently reduced overpotential of A1 for this reaction severely inhibit the efficacy of the heterojunction. As such the templated materials appear to operate primarily through the donor component, meaning any charge separation benefits provided by the heterojunction are rendered irrelevant at this higher pH.

Interestingly the donor material subjected to templating conditions without any acceptor monomers, D1Knov had HER of 17 μmol h^{-1}, higher than normal untreated D1, although still significantly lower than T1 and T1-75 (Figure S39, Supporting Information). This increase was observed on two separate batches of D1, with very similar increases in activity before and after Knoevenagel conditions. We speculated that the higher reaction temperatures that the D1-Knov was subjected to, may lead to a more crystalline structure and thus increased charge-transport properties but little change was seen by PXRD (Figure S12, Supporting Information). It was noted that D1-Knov was more dispersible than D1 and therefore the increase in activity may be the result of exfoliation of the D1 sheets in the highly solubilizing, high-temperature solvent mixture used for the Knoevenagel reaction. In support of this hypothesis, dynamic light scattering (DLS) analysis of D1 and D1-Knov (Figure S17, Supporting Information) shows a significant decrease in particle size after the Knoevenagel conditions.

The sensitivity of heterojunction formation to the donor:acceptor isostructural match was probed by attempting to template A1 onto the alternative 2D donor polymers, D2 and D3 (**Figure 5**.). The resultant materials T2.1 and T3.1, which contained a 50:50 donor-to-acceptor ratio, were found to have significantly lower HER than T1. D2, which utilized a shorter dianisidine linker than D1, was found to have a high HER of 19 μmol h^{-1} as a single component but only a small 18% increase in HER to 23 μmol h^{-1} when A1 was templated onto the surface. In contrast, D3 had a low activity of 2.7 μmol h^{-1} as a single component, and whilst this number did increase significantly to 9.7 μmol h^{-1} upon templation of A1, this equates to T3.1 essentially displaying the same activity as the acceptor alone (9.4 μmol h^{-1}). D2 and D3 both have suitable FMOs (Figure S27, Supporting Information) to provide a type II heterojunction with A1 but do not have matching tecton confirmation so these results indicate that the misalignment of aromatic units leads to less idealized π-stacking and potentially to a less well-organized interface between the donor and acceptor components. There seemed to be no particular correlation between Pt photodeposition yield and polymer pore size. The smaller pored D2 and larger pored D3 both had slightly higher Pt loadings than D1 (2.94 and 2.67 respectively compared to 2.39 wt%). The templates

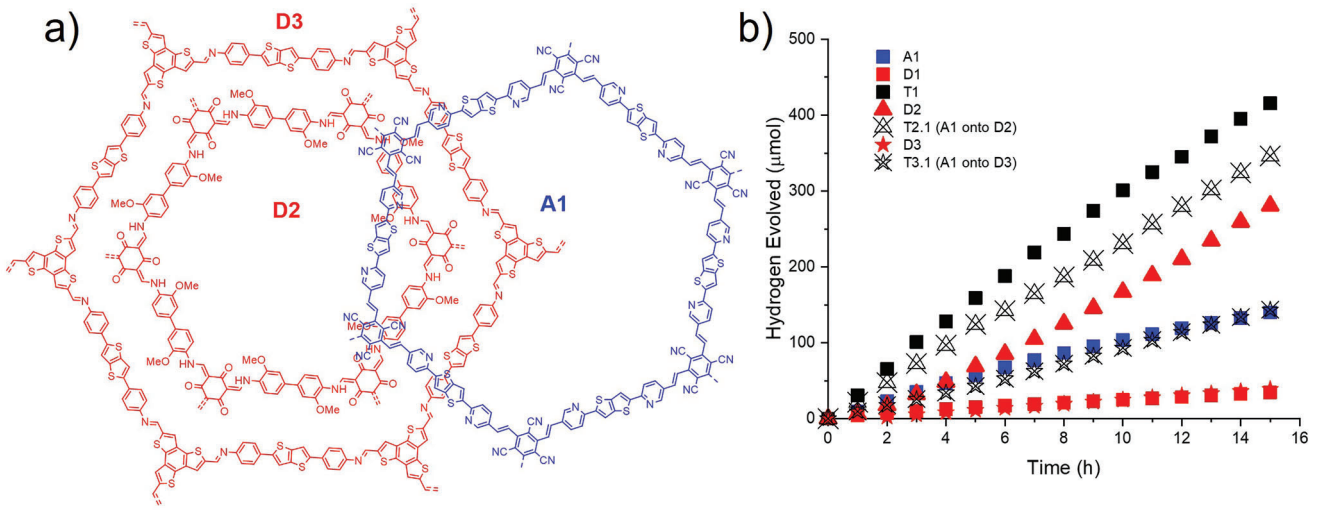

Figure 5. a) Chemical structures of the alternative donor polymers. b) Photocatalytic hydrogen production of the polymers (5 mg) with 3 wt% Pt dispersed in DMF:water (2:5, 35 mL) with ascorbic acid (440 mg) under visible-light illumination.

of these alternative donors with A1, T2.1, and T3.1, also showed similar Pt deposition with 2.62 and 2.51 wt% Pt compared to the original T1 template's 2.23 wt%.

The IP of D1 is too shallow to facilitate water oxidation. However, some overall water-splitting systems employ a two-semiconductor approach and utilize a Z-scheme whereby a hydrogen evolution catalyst is coupled to a separate oxygen evolution catalyst.[7] This coupling can be achieved through direct contact,[70] solid-state electron mediators,[71,72] or solution-based redox shuttles.[73] Whilst the yield of charge carriers on T1 is increased in the presence of ascorbic acid, it was thought that the more accessible charge-separated states in this material in comparison to the single components may facilitate oxidation of a wider range of hole scavengers. As such, the templated material was tested for proton reduction with 3 wt% Pt in the presence of electron donors that have been proven to be active as reversible redox shuttles in Z-scheme systems for overall water splitting.[7] Using $FeCl_2$ as the electron donor T1 produced hydrogen at an initial rate of 0.03 μmol h^{-1} whilst using NaI produced 0.14 μmol h^{-1} (Figure S40, Supporting Information). When the electron donor was switched to $[Co(phen)_3]Cl_2$,[74] T1 produced hydrogen at a much higher rate of 0.44 μmol h^{-1} over the first four hours (Figure S41, Supporting Information). Hydrogen evolution from all systems started to plateau between 1 and 5 h, most likely due to the build-up of Fe^{3+}, IO_3^- and Co^{3+} ions respectively. These species are more susceptible to oxidation than protons and so inhibit hydrogen evolution. This tailing-off effect is frequently observed when testing one "half" of a Z-scheme reaction and is why the starting concentrations of the oxidized and reduced shuttle species, as well as the relative concentration of hydrogen evolution catalyst and oxygen evolution catalyst crucial to Z-scheme efficacy.[73] All systems were tested at pH 4, so should have sufficient overpotential for A1 to drive proton reduction. The IP of D1 also lies >0.5 V lower than the $Co(phen)_3^{2+}$ oxidation potential, however, it is possible that the smaller (<0.15 eV) driving potential for Fe^{2+} and I^- oxidation (Table S1, Supporting Information) by D1 leads to the lower rate in these cases. Interestingly when the single component polymers were tested with the $[Co(phen)_3]Cl_2$ electron donor A1 showed negligible hydrogen production but D1 showed a rate of 0.18 μmol h^{-1}. This is in contrast to the rates with ascorbic acid, where A1 had higher activity, as well as the yield of photogenerated charges observed by TAS. The trend, using the alternative $[Co(phen)_3]Cl_2$ electron donor, could perhaps be indicative of the inaccessibility of the charges generated on A1 in comparison to D1, which in both the template and as a single component appears to be more efficient at transfer of holes from the semiconductor to the reductant. This may be more crucial in systems using the low electron donor concentrations (≈1 mmol L^{-1}) required for reversible redox mediator hole quenching as opposed to systems that use the higher concentrations associated with sacrificial hole quenching (>100 mmol L^{-1}).

3. Conclusion

A templated polymer photocatalyst with improved hydrogen evolution rates has been generated by combining donor and acceptor components in a templated growth method. The isostructural match of the donor and acceptor components was found to be crucial for improvement in photocatalytic activity, with a more than 3-fold enhancement of the heterojunction material for donor and acceptor components with matching tecton conformation. Photophysical characterization of polymer dispersions by TAS revealed faster charge separation in the templated material due to the heterojunction interface, yielding long-lived charges (up to millisecond timescale). Crucially these charges are also efficiently extracted upon the addition of Pt co-catalyst and ascorbic acid, suggesting they were responsible for the difference in the photocatalytic activity in templated polymer relative to neat donor and acceptor polymers. The difference in charge extraction between the templated material and its acceptor component indicates the benefit of the heterojunction interface in reducing charge trapping to deep states, a common limiting factor in the photocatalytic activity of 2D polymer photocatalysts such as carbon nitride.[33,75] Provided donor and acceptor components with

the relative energy levels to form type II heterojunctions and the absolute energy levels to facilitate redox reactions can be developed, the templating route in this work should be applicable to a wide range of 2D materials. This could result in COFs, CTFs, or other promising layered photocatalysts with improved charge separation and extraction. Of particular interest would be materials with slightly shallowed acceptor EA to allow for proton reduction at a wider range of pHs. This is particularly important for moving toward Z-scheme systems which are highly pH dependent. The results of T1 with the various redox mediators were highly encouraging however; The HER with the cobalt mediator corresponds to 172 μmol $h^{-1}g^{-1}$ and is higher than the 120 μmol $h^{-1}g^{-1}$ obtained from a Ru-$SrTiO_3$:Rh hydrogen evolution catalyst using the same electron donor (albeit at different starting pH and using different cocatalysts). Interestingly, HEC could be effectively employed in a Z-scheme when coupled with a $BiVO_4$ OEC.[74] Further studies will therefore pair T1 with a variety of OEC catalysts to facilitate redox-mediated overall water splitting.

4. Experimental Section

Synthesis of 4,4′-(Thieno[3,2-b]thiophene-2,5-diyl)dianiline, M2: 2,5-Dibromothieno[3,2-b]thiophene (1.49 g, 5.0 mmol), (4,4,5,5-tetramethyl-1,3,2-dioxaborolan-2-yl)aniline (2.57 g, 11.7 mmol), toluene (200 mL), $K_2CO_{3(aq)}$ (50 mL, 2 M) and Starks' catalyst (2 drops) were added to a flask and degassed by nitrogen bubbling for 30 minutes. $Pd(PPh_3)_4$ (100 mg, 1.73 mol%) was added and the mixture was further degassed for 5 min before being heated at 100 °C for 16 h under nitrogen, with stirring. After cooling the mixture was poured into methanol (500 mL) and stirred for 30 min. The precipitate was collected by filtration and washed with water (200 mL), more methanol (200 mL), and chloroform (100 mL). The crude material was recrystallized in DMF/diethyl ether and dried under vacuum to give the product as a yellow-green powder (1.1 g, 68%). ^{1}H NMR (400 MHz, DMSO-d_6): δ (ppm) = 7.48 (s, 2H), 7.34 (d, J = 7 Hz, 4H), 6.61 (d, J = 7 Hz, 4H), 5.37 (s, 4H). ^{13}C NMR (400 MHz, DMSO-d_6): δ (ppm) = 148.8, 145.3, 136.8, 126.2, 121.8, 114.1, 112.8. HR-MS Calcd for $[C_{18}H_{14}N_2S_2]$+: m/z = 322.0593; Found: m/z = 322.0597.

Synthesis of 6,6′-(Thieno[3,2-b]thiophene-2,5-diyl)dinicotinaldehyde, M4: 2,5-Bis(trimethylstannyl)thieno[3,2-b]thiophene (466 mg, 1.0 mmol), 6-bromonicotinaldehyde (409 mg, 2.2 mmol) and $Pd(PPh_3)_4$ (58 mg, 5 mol%) were dried under vacuum. In a separate flask, DMF (50 mL) was degassed by nitrogen bubbling for 30 min before addition to the monomers. The mixture was heated by stirring at 120 °C for 16 h under nitrogen. After cooling the mixture was poured into acetonitrile (200 mL) and stirred for 30 min. The precipitate was collected by filtration and washed with methanol (100 mL), hexane (100 mL), and DCM (100 mL). The crude material was recrystallized from DMF/DCM and dried under vacuum to give the product as a bright orange powder. (320 mg, 91%). ^{1}H NMR (400 MHz, $C_2D_2Cl_4$): δ (ppm) = 10.38 (s, 2H), 9.34 (s, 2H), 8.52 (d, J = 8.3 Hz, 2H), 8.36 (s, 2H), 8.18 (d, J = 8.3 Hz, 2H). The solubility of M4 was too low for ^{13}C NMR analysis and HR-MS.

Synthesis of D1: M1 (33.6 mg, 0.16 mmol), M2 (77.4 mg, 0.24 mmol), mesitylene (4.5 mL), and 1,4-dioxane (4.5 mL) were added to a Schlenk tube, and sonicated until well dispersed. Acetic acid (0.8 mL, 6 M) was added and the tube was immediately frozen in liquid nitrogen. The mixture was degassed by three cycles of freeze–pump–thaw before filling with nitrogen, sealing, and heating to 120 °C for 3 days with stirring. The mixture was poured into THF (100 mL) and stirred for 30 min. The red precipitate was collected by filtration (0.2 μm nylon membrane) and washed with more THF (100 mL), methanol (100 mL), and chloroform (100 mL). The solid was resuspended in acetone (100 mL), stirred for 1 h, and collected by filtration. This step was repeated three times before drying the solid under a vacuum at 80 °C overnight to give D1 as a red powder (78 mg, 76%).

Synthesis of A1: M3 (19.5 mg, 0.10 mmol), M4 (52.6 mg, 0.15 mmol), DMF (4.5 mL), and *o*-dichlorobenzene (4.5 mL) were added to a Schlenk tube and sonicated until well dispersed. piperidine (0.15 mL) was added and the tube was immediately frozen in liquid nitrogen. The mixture was degassed by 3 cycles of freeze–pump–thaw before filling with nitrogen, sealing, and heating to 180 °C for 24 h with stirring. The mixture was poured into chloroform (100 mL) and stirred for 30 min. The red precipitate was collected by filtration (0.2 μm poly(tetrafluoroethylene) (PTFE) membrane) and washed with more chloroform (200 mL). The solid was resuspended in acetone (100 mL), stirred for 1 h, and collected by filtration. This step was repeated three times before drying the solid under a vacuum at 80 °C overnight to give A1 as a red powder (64 mg, 96%).

Synthesis of T1: D1 (33 mg), M3 (9.8 mg, 0.05 mmol), M4 (26.3 mg, 0.075 mmol), DMF (4.5 mL), and *o*-dichlorobenzene (4.5 mL) were added to a Schlenk tube and sonicated until well dispersed. piperidine (0.1 mL) was added and the tube was immediately frozen in liquid nitrogen. The mixture was degassed by three cycles of freeze–pump–thaw before filling with nitrogen, sealing, and heating to 180 °C for 24 h with stirring. The mixture was poured into chloroform (100 mL) and stirred for 30 min. The red precipitate was collected by filtration (0.2 μm PTFE membrane) and washed with more chloroform (200 mL). The solid was resuspended in acetone (100 mL), stirred for 1 h, and collected by filtration. This step was repeated three times before drying the solid under vacuum at 80 °C overnight to give T1 as a red powder (63 mg, 90% wrt Knoevenagel).

Photocatalytic Testing: Preparation of samples with ascorbic acid hole scavenger: Polymer (5 mg) was sonicated in DMF (10 mL) for 5 min until well dispersed. This suspension was injected into the bottom of a vial containing ascorbic acid (440 mg) and water (25 mL) whilst sonicating. PtH_2Cl_6 (0.8 wt% aqueous solution, 39 μL) was added and the dispersion was sonicated for a further 5 min. For samples tested with varied ascorbic acid concentrations or Pt loadings, the amount of ascorbic acid or PtH_2C_{l6} was adjusted accordingly. For samples tested with varied co-solvent, the DMF was replaced with water or NMP. For samples tested at pH 7 $NaOH_{(aq)}$ (4 M) was added dropwise to the ascorbic acid solution until pH 7 before injection of the DMF suspension.

Photocatalytic Testing: Preparation of [Co(phen)$_3$]Cl$_2$ Solution: 1,10-Phenathroline (54.6 mg, 0.3 mmol), and Cobalt chloride hexahydrate (23.8 mg, 0.1 mmol) were dissolved in water (9 mL). $HCl_{(aq)}$ (4 M) was added dropwise until pH 3 and the solution was made up to 10 mL with more water.

Photocatalytic Testing: Preparation of Samples with Co Redox Shuttles: Polymer (2.5 mg) was sonicated in water (31.5 mL) for 5 min until well dispersed, Co redox shuttle solution (3.5 mL, 10 mmol L^{-1}) and PtH_2Cl_6 (0.8 wt% aqueous solution, 19 μL) were added and the dispersion sonicated for a further 5 minutes.

Supporting Information

Supporting Information is available from the Wiley Online Library or from the author.

Acknowledgements

The authors would like to acknowledge financial support from KAUST Office of Sponsored Research CRG10, by EU Horizon 2020 grant agreement n°952911, BOOSTER, grant agreement n°862474, RoLA-FLEX, and grant agreement n°101007084 CITYSOLAR, as well as EPSRC Projects EP/T026219/1 and EP/W017091/1. This project received funding from the European Union's Horizon 2020 research and innovation program under the Marie Sklodowska-Curie grant agreement no. 886664 (S.G.-C.), and China Scholarhip Council-Imperial Scholarship (S.Y.). The authors acknowledge the David Cockayne Centre for Electron Microscopy at University of Oxford for access to equipment financially supported by the EPSRC (EP/K040375/1 "South of England Analytical Electron Microscope") and the Henry Royce Institute for Advanced Materials (EP/R00661X/1, EP/S019367/1, EP/R010145/1).

Conflict of Interest

The authors declare no conflict of interest.

Data Availability Statement

The data that support the findings of this study are available from the corresponding author upon reasonable request.

Keywords

2D polymers, heterojunctions, organic semiconductors, photocatalysis, solar fuels

Received: January 2, 2023
Revised: March 28, 2023
Published online:

[1] M. Gray, S. Sundaresan, B. Udomchaiporn, S. Lavelle, L. Chau, *Carbon Tracker Initiative*, London, UK **2020**.
[2] International Renewable Energy Agency (2019), Renewable Power Generation Costs in 2018.
[3] X. Wang, K. Maeda, A. Thomas, K. Takanabe, G. Xin, J. M. Carlsson, K. Domen, M. Antonietti, *Nat. Mater.* **2009**, *8*, 76.
[4] M. Z. Rahman, M. G. Kibria, C. B. Mullins, *Chem. Soc. Rev.* **2020**, *49*, 1887.
[5] Y. Wang, A. Vogel, M. Sachs, R. S. Sprick, L. Wilbraham, S. J. A. Moniz, R. Godin, M. A. Zwijnenburg, J. R. Durrant, A. I. Cooper, J. Tang, *Nat. Energy* **2019**, *4*, 746.
[6] A. Fujishima, K. Honda, *Nature* **1972**, *238*, 37.
[7] S. Chen, T. Takata, K. Domen, *Nat. Rev. Mater.* **2017**, *2*, 17050.
[8] T. Takata, J. Jiang, Y. Sakata, M. Nakabayashi, N. Shibata, V. Nandal, K. Seki, T. Hisatomi, K. Domen, *Nature* **2020**, *581*, 411.
[9] J. Wen, J. Xie, X. Chen, X. Li, *Appl. Surf. Sci.* **2017**, *391*, 72.
[10] Y. Zhang, J. Liu, G. Wu, W. Chen, *Nanoscale* **2012**, *4*, 5300.
[11] G. Zhang, L. Lin, G. Li, Y. Zhang, A. Savateev, S. Zafeiratos, X. Wang, M. Antonietti, *Angew. Chem., Int. Ed.* **2018**, *57*, 9372.
[12] D. J. Martin, K. Qiu, S. A. Shevlin, A. D. Handoko, X. Chen, Z. Guo, J. Tang, *Angew. Chem., Int. Ed.* **2014**, *53*, 9240.
[13] L. Lin, H. Ou, Y. Zhang, X. Wang, *ACS Catal.* **2016**, *6*, 3921.
[14] G. Zhang, G. Li, Z. A. Lan, L. Lin, A. Savateev, T. Heil, S. Zafeiratos, X. Wang, M. Antonietti, *Angew. Chem., Int. Ed.* **2017**, *56*, 13445.
[15] M. G. Schwab, M. Hamburger, X. Feng, J. Shu, H. W. Spiess, X. Wang, M. Antonietti, K. Müllen, *Chem. Commun.* **2010**, *46*, 8932.
[16] R. S. Sprick, J. X. Jiang, B. Bonillo, S. Ren, T. Ratvijitvech, P. Guiglion, M. A. Zwijnenburg, D. J. Adams, A. I. Cooper, *J. Am. Chem. Soc.* **2015**, *137*, 3265.
[17] J. Bi, W. Fang, L. Li, J. Wang, S. Liang, Y. He, M. Liu, L. Wu, *Macromol. Rapid Commun.* **2015**, *36*, 1799.
[18] L. Li, Z. Cai, Q. Wu, W.-Y. Lo, N. Zhang, L. X. Chen, L. Yu, *J. Am. Chem. Soc.* **2016**, *138*, 7681 .
[19] C. Yang, B. C. Ma, L. Zhang, S. Lin, S. Ghasimi, K. Landfester, K. A. I. Zhang, X. Wang, *Angew. Chem., Int. Ed.* **2016**, *55*, 9202.
[20] R. S. Sprick, B. Bonillo, R. Clowes, P. Guiglion, N. J. Brownbill, B. J. Slater, F. Blanc, M. A. Zwijnenburg, D. J. Adams, A. I. Cooper, *Angew. Chem., Int. Ed.* **2016**, *55*, 1792.
[21] L. Stegbauer, K. Schwinghammer, B. V. Lotsch, *Chem. Sci.* **2014**, *5*, 2789.
[22] V. S. Vyas, F. Haase, L. Stegbauer, G. Savasci, F. Podjaski, C. Ochsenfeld, B. V. Lotsch, *Nat. Commun.* **2015**, *6*, 8508.
[23] X. Wang, L. Chen, S. Y. Chong, M. A. Little, Y. Wu, W.-H. Zhu, R. Clowes, Y. Yan, M. A. Zwijnenburg, R. S. Sprick, A. I. Cooper, *Nat. Chem.* **2018**, *10*, 1180.
[24] E. Jin, Z. Lan, Q. Jiang, K. Geng, G. Li, X. Wang, D. Jiang, *Chem* **2019**, *5*, 1632.
[25] L. Wang, R. Fernández-Terán, L. Zhang, D. L. A. Fernandes, L. Tian, H. Chen, H. Tian, *Angew. Chem., Int. Ed.* **2016**, *55*, 12306.
[26] W. Huang, Z. J. Wang, B. C. Ma, S. Ghasimi, D. Gehrig, E. Laquai, K. Landfester, K. A. I. Zhang, *J. Mater. Chem. A* **2016**, *4*, 7555.
[27] M. Sachs, R. S. Sprick, D. Pearce, S. A. J. Hillman, A. Monti, A. A. Y. Guilbert, N. J. Brownbill, S. Dimitrov, X. Shi, F. Blanc, M. A. Zwijnenburg, J. Nelson, J. R. Durrant, A. I. Cooper, *Nat. Commun.* **2018**, *9*, 4968.
[28] Z. Hu, Z. Wang, X. Zhang, H. Tang, X. Liu, F. Huang, Y. Cao, *iScience* **2019**, *13*, 33.
[29] R. S. Sprick, C. M. Aitchison, E. Berardo, L. Turcani, L. Wilbraham, B. M. Alston, K. E. Jelfs, M. A. Zwijnenburg, A. I. Cooper, *J. Mater. Chem. A* **2018**, *6*, 11994.
[30] C. Li, J. Liu, H. Li, K. Wu, J. Wang, Q. Yang, *Nat. Commun.* **2022**, *13*, 2357.
[31] M. Schröder, K. Kailasam, J. Borgmeyer, M. Neumann, A. Thomas, R. Schomäcker, M. Schwarze, *Energy Technol.* **2015**, *3*, 1014.
[32] S. Roy, E. Reisner, *Angew. Chem., Int. Ed.* **2019**, *58*, 12180.
[33] R. Godin, Y. Wang, M. A. Zwijnenburg, J. Tang, J. R. Durrant, *J. Am. Chem. Soc.* **2017**, *139*, 5216.
[34] S. Corby, R. R. Rao, L. Steier, J. R. Durrant, *Nat. Rev. Mater.* **2021**, *6*, 1136.
[35] R. Godin, J. R. Durrant, *Chem. Soc. Rev.* **2021**, *50*, 13372.
[36] S. Jin, M. Supur, M. Addicoat, K. Furukawa, L. Chen, T. Nakamura, S. Fukuzumi, S. Irle, D. Jiang, *J. Am. Chem. Soc.* **2015**, *137*, 7817.
[37] F. Liu, Y. He, X. Liu, Z. Wang, H.-L. Liu, X. Zhu, C.-C. Hou, Y. Weng, Q. Zhang, Y. Chen, *Chem. Commun.* **2022**, *58*, 13210.
[38] L. Guo, Y. Niu, S. Razzaque, B. Tan, S. Jin, *ACS Catal.* **2019**, *9*, 9438.
[39] Z.-A. Lan, X. Chi, M. Wu, X. Zhang, X. Chen, G. Zhang, X. Wang, Z.-A. Lan, X. Chi, M. Wu, X. Zhang, X. Chen, G. Zhang, X. Wang, *Small* **2022**, *18*, 2200129.
[40] T. Feng, D. Streater, B. Sun, K. Duisenova, D. Wang, Y. Liu, J. Huang, J. Zhang, *J. Phys. Chem. Lett.* **2022**, *13*, 1398.
[41] L. Li, Z. Cai, Q. Wu, W.-Y. Lo, N. Zhang, L. X. Chen, L. Yu, *J. Am. Chem. Soc.* **2016**, *138*, 7681.
[42] Y. S. Kochergin, D. Schwarz, A. Acharjya, A. Ichangi, R. Kulkarni, P. Eliášová, J. Vacek, J. Schmidt, A. Thomas, M. J. Bojdys, *Angew. Chem., Int. Ed.* **2018**, *57*, 14188.
[43] S. Karuthedath, J. Gorenflot, Y. Firdaus, N. Chaturvedi, C. S. P. De Castro, G. T. Harrison, J. I. Khan, A. Markina, A. H. Balawi, T. A. Dela Peña, W. Liu, R. Z. Liang, A. Sharma, S. H. K. Paleti, W. Zhang, Y. Lin, E. Alarousu, D. H. Anjum, P. M. Beaujuge, S. De Wolf, I. McCulloch, T. D. Anthopoulos, D. Baran, D. Andrienko, F. Laquai, *Nat. Mater.* **2020**, *20*, 378.
[44] A. Liu, L. Gedda, M. Axelsson, M. Pavliuk, K. Edwards, L. Hammarström, H. Tian, *J. Am. Chem. Soc.* **2021**, *143*, 2875.
[45] H. Yang, X. Li, R. S. Sprick, A. I. Cooper, *Chem. Commun.* **2020**, *56*, 6790.
[46] J. Kosco, M. Bidwell, H. Cha, T. Martin, C. T. Howells, M. Sachs, D. H. Anjum, S. G. Lopez, L. Zou, A. Wadsworth, W. Zhang, L. Zhang, J. Tellam, R. Sougrat, F. Laquai, D. M. DeLongchamp, J. R. Durrant, I. McCulloch, *Nat. Mater.* **2020**, *19*, 559.
[47] J. Kosco, S. Gonzalez-Carrero, C. T. Howells, T. Fei, Y. Dong, R. Sougrat, G. T. Harrison, Y. Firdaus, R. Sheelamanthula, B. Purushothaman, F. Moruzzi, W. Xu, L. Zhao, A. Basu, S. De Wolf, T. D. Anthopoulos, J. R. Durrant, I. McCulloch, *Nat. Energy* **2022**, *7*, 340.
[48] N. C. Flanders, M. S. Kirschner, P. Kim, T. J. Fauvell, A. M. Evans, W. Helweh, A. P. Spencer, R. D. Schaller, W. R. Dichtel, L. X. Chen, *J. Am. Chem. Soc.* **2020**, *142*, 14957.

[49] M. Leng, L. Fang, *Chem* **2022**, *8*, 2904.
[50] D. Bessinger, L. Ascherl, F. Auras, T. Bein, *J. Am. Chem. Soc.* **2017**, *139*, 12035.
[51] N. A. A. Zwaneveld, R. Pawlak, M. Abel, D. Catalin, D. Gigmes, D. Bertin, L. Porte, *J. Am. Chem. Soc.* **2008**, *130*, 6678.
[52] L. Grill, M. Dyer, L. Lafferentz, M. Persson, M. V. Peters, S. Hecht, *Nat. Nanotechnol.* **2007**, *2*, 687.
[53] S. Clair, O. Ourdjini, M. Abel, L. Porte, *Adv. Mater.* **2012**, *24*, 1252.
[54] K. Yuan, P. Guo-Wang, T. Hu, L. Shi, R. Zeng, M. Forster, T. Pichler, Y. Chen, U. Scherf, *Chem. Mater.* **2015**, *27*, 7403.
[55] J. W. Colson, A. R. Woll, A. Mukherjee, M. P. Levendorf, E. L. Spitler, V. B. Shields, M. G. Spencer, J. Park, W. R. Dichtel, *Science* **2011**, *332*, 228.
[56] A. M. Evans, L. R. Parent, N. C. Flanders, R. P. Bisbey, E. Vitaku, M. S. Kirschner, R. D. Schaller, L. X. Chen, N. C. Gianneschi, W. R. Dichtel, *Science* **2018**, *361*, 52.
[57] E. Jin, K. Geng, K. H. Lee, W. Jiang, J. Li, Q. Jiang, S. Irle, D. Jiang, *Angew. Chem., Int. Ed.* **2020**, *59*, 12162.
[58] S. Kandambeth, A. Mallick, B. Lukose, M. V. Mane, T. Heine, R. Banerjee, *J. Am. Chem. Soc.* **2012**, *134*, 19524.
[59] J. Bertrandie, J. Han, C. S. P. De Castro, E. Yengel, J. Gorenflot, T. Anthopoulos, F. Laquai, A. Sharma, D. Baran, *Adv. Mater.* **2022**, *34*, 22023575.
[60] Z. Zhang, Y. Chen, L. Zhou, C. Chen, Z. Han, B. Zhang, Q. Wu, L. Yang, L. Du, Y. Bu, P. Wang, X. Wang, H. Yang, Z. Hu, *Nat. Commun.* **2019**, *10*, 1657.
[61] C. M. Aitchison, C. M. Kane, D. P. McMahon, P. R. Spackman, A. Pulido, X. Wang, L. Wilbraham, L. Chen, R. Clowes, M. A. Zwijnenburg, R. S. Sprick, M. A. Little, G. M. Day, A. I. Cooper, *J. Mater. Chem. A* **2020**, *8*, 7158.
[62] J. Kosco, M. Sachs, R. Godin, M. Kirkus, L. Francas, M. Bidwell, M. Qureshi, D. Anjum, J. R. Durrant, I. McCulloch, *Adv. Energy Mater.* **2018**, *8*, 1802181.
[63] S. Haldar, D. Chakraborty, B. Roy, G. Banappanavar, K. Rinku, D. Mullangi, P. Hazra, D. Kabra, R. Vaidhyanathan, *J. Am. Chem. Soc.* **2018**, *140*, 13367.
[64] H. Chen, Z. G. Gu, J. Zhang, *J. Am. Chem. Soc.* **2022**, *144*, 7245.
[65] J. Kosco, S. Gonzalez-Carrero, C. T. Howells, W. Zhang, M. Moser, R. Sheelamanthula, L. Zhao, B. Willner, T. C. Hidalgo, H. Faber, B. Purushothaman, M. Sachs, H. Cha, R. Sougrat, T. D. Anthopolous, S. Inal, J. R. Durrant, I. McCulloch, *Adv. Mater.* **2021**, *34*, 2105007.
[66] H. Kasap, C. A. Caputo, B. C. M. Martindale, R. Godin, V. W. H. Lau, B. V. Lotsch, J. R. Durrant, E. Reisner, *J. Am. Chem. Soc.* **2016**, *138*, 9183.
[67] Y. Li, L. Yang, H. He, L. Sun, H. Wang, X. Fang, Y. Zhao, D. Zheng, Y. Qi, Z. Li, W. Deng, *Nat. Commun.* **2022**, *13*, 1355.
[68] S. Ma, T. Deng, Z. Li, Z. Zhang, J. Jia, Q. Li, G. Wu, H. Xia, S.-W. Yang, X. Liu, *Angew. Chem., Int. Ed.* **2022**, *134*, 202208919.
[69] C. Shu, C. Han, X. Yang, C. Zhang, Y. Chen, S. Ren, F. Wang, F. Huang, J.-X. Jiang, C. Shu, C. Han, C. Zhang, Y. Chen, J. Jiang, X. Yang, F. Huang, S. Ren, F. Wang, *Adv. Mater.* **2021**, *33*, 2008498.
[70] B. Dong, J. Cui, Y. Gao, Y. Qi, F. Zhang, C. Li, *Adv. Mater.* **2019**, *31*, 1808185.
[71] Q. Wang, T. Hisatomi, Q. Jia, H. Tokudome, M. Zhong, C. Wang, Z. Pan, T. Takata, M. Nakabayashi, N. Shibata, Y. Li, I. D. Sharp, A. Kudo, T. Yamada, K. Domen, *Nat. Mater.* **2016**, *15*, 611.
[72] Q. Wang, T. Hisatomi, Y. Suzuki, Z. Pan, J. Seo, M. Katayama, T. Minegishi, H. Nishiyama, T. Takata, K. Seki, A. Kudo, T. Yamada, K. Domen, *J. Am. Chem. Soc.* **2017**, *139*, 24.
[73] K. Maeda, *ACS Catal.* **2013**, *3*, 1486.
[74] Y. Sasaki, H. Kato, A. Kudo, *J. Am. Chem. Soc.* **2013**, *135*, 5441.
[75] E. Mitchell, A. Law, R. Godin, *J. Photochem. Photobiol. C: Photochem. Rev.* **2021**, *49*, 100453.